

Contributions of quasifission and fusion-fission in the $^{24}\text{Mg} + ^{178}\text{Hf}$ reaction at 145 MeV laboratory beam energy using the Boltzmann-Uehling-Uhlenbeck model

Yujie Feng , Yingge Huang , Erxi Xiao, Xin Lei, Long Zhu, and Jun Su *

Sino-French Institute of Nuclear Engineering and Technology, Sun Yat-sen University, Zhuhai 519082, China



(Received 28 November 2022; accepted 5 April 2023; published 13 April 2023)

Background: Understanding the mechanism of the quasifission reaction is important, because it is an essential competitor to the fusion reaction leading to superheavy elements. However, it is a challenge to separate the quasifission and fusion-fission components.

Purpose: This paper provides a dynamics description of the $^{24}\text{Mg} + ^{178}\text{Hf}$ reaction at laboratory beam energy of 145 MeV, and studies contributions of quasifission and fusion-fission in the reaction.

Method: The Boltzmann-Uehling-Uhlenbeck model is improved to study the heavy-ion collision at incident energy near the Coulomb barrier. A method is developed to determine the window of the dinuclear system during the evolution.

Results: It is shown that the fusion occurs with a large percentage in the central collision, and the quasiinelastic scattering occurs mainly in the peripheral collision. The quasifission competes with the fusion in collisions with small impact parameters. It is found that the cross sections of quasifission decrease and those of fusion increase with increasing surface energy or incompressibility. The mass-angular correlation of the quasifission events shows the mass asymmetry. The fragments emitted at the front angle are targetlike fragments and those at the back angle are projectilelike fragments. Furthermore, the differential cross sections at the angles 0° and 180° are larger than that at 90° .

Conclusions: By comparing the calculations of the mass distribution and mass-angular correlation to the data, it is deduced that the compound nucleus fission plays a main role and accounts for the characteristic of fragment observables in the $^{24}\text{Mg} + ^{178}\text{Hf}$ reaction at laboratory beam energy of 145 MeV.

DOI: [10.1103/PhysRevC.107.044606](https://doi.org/10.1103/PhysRevC.107.044606)

I. INTRODUCTION

The pursuit of synthesizing superheavy elements promotes expanding the knowledge of the microscopic dynamics of the dinuclear system during nuclear reactions near the Coulomb barrier [1]. The dinuclear system in the dissipation process can follow two paths, i.e., forming a compact compound nucleus and fusing or splitting apart again before reaching a compact equilibrium shape [2,3]. This latter process is known as a fissionlike reaction outcome in which no compound nucleus is formed, and is referred to as a quasifission (QF) reaction [4]. The QF reaction competes with the fusion reaction leading to superheavy elements [5]. Therefore, understanding the mechanism of the QF reaction is crucial in determining an optimal scheme for synthesizing new superheavy elements [6–8].

Since the discovery of QF, numerous experimental and theoretical studies have been conducted to understand its underlying mechanisms [9]. QF has been experimentally identified in a mixture of QF and fission events by various methods such as measuring γ rays [10], mass-angular correlation [11], mass-energy distribution [12,13], and others. It has been found that QF depends on several factors, including reaction energy [14], nuclear deformation [15], and neutron-proton

ratio [16]. Several theoretical models have been developed to describe QF reactions, ranging from macroscopic dynamics models like the dinuclear system (DNS) model [17,18] and the dynamical cluster-decay model (DCM) [19,20], to microscopic dynamics models such as the time-dependent Hartree-Fock (TDHF) theory [21,22], quantum molecular dynamics (QMD) theories [23], and the stochastic mean-field (SMF) approach [24]. The DNS model has successfully calculated properties such as charge, mass, and the energy distribution of QF products [25,26], while the DCM model has discovered the impact of noncoplanar degrees of freedom on QF contributions [27]. The TDHF model provides a quantum framework to study the many-body system at a full microscopic level and has been successfully applied to describe low-energy nuclear reactions, including fusion reactions, nucleon transfer, quasi-inelastic collisions, and the QF process [28–30].

The improved quantum molecular dynamics (ImQMD) model and the SMF model are well-suited semiclassical frameworks for studying the dissipation and fluctuation in the QF process [31,32]. Previous research has shown that the SMF model is particularly useful for analyzing window dynamics, including the fluctuation mechanism underlying collective motion [33].

Microscopic dynamics models have focused heavily on understanding the dissipation that occurs during the QF process.

*sujun3@mail.sysu.edu.cn

It is widely believed that there are two primary mechanisms responsible for energy dissipation in nuclear reactions: one-body and two-body dissipation. In heavy-ion collisions above the Fermi energy, two-body dissipation, which arises from nucleon-nucleon collisions, is considered to be crucial [34]. At low energies, however, the inhibition of nucleon-nucleon collisions by the Pauli principle means that one-body dissipation is generally thought to be the main driver of collective motion damping [35]. One-body dissipation contains both wall dynamics, which describes interactions between individual nucleons influenced by the mean field created by all other nucleons, and window dynamics, which refers to a small opening connecting two distinct systems. [36]. At the point when the neck is smaller than a critical size, the window dynamics can be used to calculate the dynamic process between two nuclei. However, how the window dynamics and wall dynamics compete for the reduction of the mean free path is still a question of debate and represents a long-term controversy [37].

In order to investigate dissipation during the QF process, it is necessary to establish a window using window dynamics [38]. The work by Wen *et al.* examined the Zr + Zr reaction at impact parameter $b = 0$ fm utilizing the ImQMD model and defined the fusion window as the $z = 0$ plane, which remained unchanged throughout the reaction process [39]. However, defining the window in noncentral collisions is more intricate. Ayik *et al.* explored window dynamics using the SMF approach with an ensemble of mean-field events [31].

The mass distribution and mass-angular distribution of fragments produced in the $^{24}\text{Mg} + ^{178}\text{Hf}$ reaction at $E_{\text{lab}} = 145$ MeV have been measured, where E_{lab} is the laboratory beam energy [40]. However, it should be noted that this is a mixture of both QF and compound nucleus fission (CNF) events, and currently there is no method that can separate these individual components [11]. In this paper, we improve the BUU (Boltzmann-Uehling-Uhlenbeck) model to concentrate on the microdynamics description of the heavy-ion collision near the Coulomb barrier. By separating the QF, fusion, and quasi-nelastic processes on an event-by-event basis, we are able to investigate the contributions of QF and fusion to the overall reaction. The paper is organized as follows. In Sec. II, we briefly describe the theoretical method. In Sec. III, we present both results and discussions. Finally, the conclusions and overviews are given in Sec. IV.

II. THEORETICAL FRAMEWORK

A. Boltzmann-Uehling-Uhlenbeck approach

In principle, the schemes of successive approximations to the original global N -body problem can be figured out by the idea of the BBGKY (Born, Bogoliubov, Green, Kirkwood, Yvon) hierarchy [41]. Truncating the first equation of the hierarchy with the Hartree-Fock approximation leads to the TDHF equation [21]

$$i\frac{\partial \hat{\rho}}{\partial t} = [\hat{h}[\hat{\rho}], \hat{\rho}], \quad (1)$$

where $\hat{\rho}$ is the one-body density matrix, and \hat{h} is the mean-field Hamiltonian. Making the hypothesis of molecular chaos,

one can solve the second equation of the hierarchy and rewrite the first equation of the hierarchy as the quantum Boltzmann equation [42,43],

$$i\frac{\partial \hat{\rho}}{\partial t} = [\hat{h}[\hat{\rho}], \hat{\rho}] + \hat{I}[\hat{\rho}], \quad (2)$$

where \hat{I} represents the collision term and comes from the solution of the second equation of the hierarchy.

For finite fermion systems, the collision term is extremely hard to handle in the quantum framework [44,45]. As a result, the semiclassical version of the Boltzmann equation is solved and is widely used:

$$\left(\frac{\partial}{\partial t} + \frac{\mathbf{p}}{m} \cdot \nabla_{\mathbf{r}} - \nabla_{\mathbf{r}} U(f) \cdot \nabla_{\mathbf{p}}\right) f(\mathbf{r}, \mathbf{p}, t) = I(f). \quad (3)$$

Here $f = f(\mathbf{r}, \mathbf{p}, t)$ is the classical phase space distribution, where \mathbf{r} is the coordinate and \mathbf{p} is the momentum. The value of $f(\mathbf{r}, \mathbf{p}, t) \Delta \mathbf{r} \Delta \mathbf{p}$ represents the number of particles within a phase space volume $\Delta \mathbf{r} \Delta \mathbf{p}$ around the point (\mathbf{r}, \mathbf{p}) . The left-hand side of the equation describes the evolution of the phase space distribution determined by the mean-field potential U , while the right-hand side in Eq. (3), is referred to as the collision term $I(f)$ of the Uehling-Uhlenbeck form, which includes Pauli blocking:

$$I(f) = \int [f'' f''' (1-f)(1-f') - f f' (1-f'')(1-f''')] \times W(\mathbf{p}, \mathbf{p}'; \mathbf{p}'', \mathbf{p}''') d\mathbf{p}' d\mathbf{p}'' d\mathbf{p}'''. \quad (4)$$

The notation $f' = f(\mathbf{r}, \mathbf{p}', t)$ (similar form for f'' and f''') is used, where the coordinate \mathbf{r} is the same if the collision between point particles is assumed. The symbol $W(\mathbf{p}, \mathbf{p}'; \mathbf{p}'', \mathbf{p}''')$ represents the transition rate of the particle pair from the initial states at momenta \mathbf{p} and \mathbf{p}' to the final states at \mathbf{p}'' and \mathbf{p}''' . It can be expressed as

$$W(\mathbf{p}, \mathbf{p}'; \mathbf{p}'', \mathbf{p}''') = \frac{d\sigma}{d\Omega} \delta(\mathbf{p} + \mathbf{p}' - \mathbf{p}'' - \mathbf{p}''') \times \delta(\epsilon + \epsilon' - \epsilon'' - \epsilon'''), \quad (5)$$

where $\frac{d\sigma}{d\Omega}$ denotes the differential cross section of the nucleon-nucleon scattering in the particle medium, ϵ and ϵ' are the single-particle energies of the particle pair in the initial states, and ϵ'' and ϵ''' are the final cases. The conservation of momentum and energy in the scattering process is reflected through the delta functions of momenta and single-particle energies. The single-particle energies represent the sum of kinetic energy and potential energy. Consequently, if the potential energy is independent of momentum, the last delta function can easily be replaced by the kinetic energy $\delta(\frac{\mathbf{p}^2}{2m} + \frac{\mathbf{p}'^2}{2m} - \frac{\mathbf{p}''^2}{2m} - \frac{\mathbf{p}'''^2}{2m})$.

In the actual numerical simulation of Eq. (3), the test particle principle is applied, which switches from a physical one-body problem for the phase space distribution $f(\mathbf{r}, \mathbf{p}, t)$ to a numerical N -body problem. Considering the case of a nucleus with N_p nucleons hitting another with N_t nucleons, the calculated value of the phase space distribution $f(\mathbf{r}, \mathbf{p}, t)$ has a huge numerical fluctuation, since the total nucleon number

TABLE I. The potential parameters to provide different incompressibility values K of isospin symmetric nuclear matter at saturation density $\rho_0 = 0.16 \text{ fm}^{-3}$.

	α (MeV)	β (MeV)	γ	K (MeV)
K200	-356.0	303.0	7/6	200
K240	-209.2	156.4	1.35	240
K271	-168.4	115.9	1.5	271

is less than 500 but the degree of freedom of the phase space is 6. By employing the test particle principle, N_{tp} systems with $(N_p + N_n)N_{tp}$ nucleons run simultaneously and communicate with each other, resulting in a decrease in the numerical fluctuation of the phase space distribution. In this work, we label these nucleons as test particles, and the typical value of N_{tp} used is 100. The application of the test particle principle leads to the formation of the Boltzmann-Uehling-Uhlenbeck (BUU) model [46], also referred to as Vlasov-Uehling-Uhlenbeck [47,48] or Landau-Vlasov models [49] in literature. This model determines the average trajectory of the phase space distribution with a given initial condition.

B. Inputs of the BUU model for nuclear system

When taking into account the isospin degree of freedom in the nuclear system, the phase space distribution can be expressed as a sum of the neutron and proton cases, i.e., $f = f_n + f_p$. The form of the Boltzmann equation for the neutron and proton remains the same, but the mean-field potential U and the differential cross section $\frac{d\sigma}{d\Omega}$ in the equation are different.

In the case of protons, the mean-field potential U described in Eq. (3) consists of both Coulomb and nuclear terms, while the Coulomb term is deemed unnecessary for neutrons. The Coulomb interaction between protons is represented by simple point charges and is calculated in each parallel ensemble. The nuclear potential for the neutron (or proton) is calculated as

$$U_{n(p)}(\rho, \delta) = \alpha \frac{\rho}{\rho_0} + \beta \frac{\rho^\gamma}{\rho_0^\gamma} + \frac{C_{sp}(\gamma_i + 1)}{2} \frac{\rho^{\gamma_i}}{\rho_0^{\gamma_i}} \delta^2 \pm \frac{C_{sp}}{2} \frac{\rho^{\gamma_i+1}}{\rho_0^{\gamma_i}} 2\delta. \quad (6)$$

In the above equation, the symbol “ \pm ” takes on a value of “+” for the neutron potential U_n and “-” for the proton potential U_p . The nucleon density ρ is calculated as the sum of the neutron density $\rho_n = \int f_n d\mathbf{p}$ and the proton density $\rho_p = \int f_p d\mathbf{p}$. The isospin asymmetry $\delta = (\rho_n - \rho_p)/\rho$ determines the isospin dependence of the potential. The parameters ρ_0 , α , β , and γ determine the equation of state (EOS) of the isospin symmetric nuclear matter. Three sets of EOS parameters are optional to provide different incompressibility K at saturation density $\rho_0 = 0.16 \text{ fm}^{-3}$; see Table I. The symmetry energy parameters are set as $C_{sp} = 40.0 \text{ MeV}$, and $\gamma_i = 0.75$.

Taking into account the isospin dependence, the differential cross sections represented by $\frac{d\sigma}{d\Omega}$ in Eq. (5) are substituted

with $(\frac{d\sigma}{d\Omega})_{jk}$. This substituted value is believed to be the direct result of the cross sections of nucleon-nucleon (NN) collisions in free space $\sigma_{jk}^{\text{free}}$, the factor of the angular distribution f_{jk}^{angl} , and the in-medium correction factor f_{jk}^{med} ,

$$\left(\frac{d\sigma}{d\Omega}\right)_{jk} = \sigma_{jk}^{\text{free}} f_{jk}^{\text{angl}} f_{jk}^{\text{med}}. \quad (7)$$

The subscripts jk are associated with different channels of the NN collision, i.e., elastic proton-proton scattering ($jk = pp$), elastic neutron-proton scattering ($jk = np$), and elastic neutron-neutron scattering ($jk = nn$). The inelastic neutron-neutron collisions have not been taken into account in this work. The parametrization of the cross sections of the NN scattering in the free space and their angular distribution is from Ref. [50], and the in-medium factor was extracted from Ref. [51].

Furthermore, the initial conditions take into account the nuclear radius and nuclear deformation of the ground state. The coordinate of the test particles is randomly sampled to fit the experimental radius and deformation parameter. The momentum is in accordance with the Fermi distribution at temperature $T = 0 \text{ MeV}$. The distance between the projectile nuclei and the target nuclei in the initial state is set to be 20 fm.

C. Improvement for studying the heavy-ion collision near the Coulomb barrier

In the conventional version of the BUU model, the NN scattering considers the Pauli blocking. In heavy-ion collisions at intermediate energies, the NN scattering is abundant. Therefore the Pauli blocking provides the basic quantum properties in the classical Boltzmann equation and leads to a semiclassical model. However, at incident energy near the Coulomb barrier, the NN scattering is sparse and the Pauli blocking does not work. To compensate for the quantum properties of the colliding system and to avoid the tendency of the evolution toward the classical phase space distribution, the phase-space-density constraint (PSDC) method is applied.

By the Pauli exclusion principle, the phase space occupation probability of a same particle must be less than 1. In principle, the phase space occupation probability is the integration of the phase space distribution over a hypercube of volume h^3 in the phase space.

$$\bar{f}_{n(p)} = \frac{1}{2} \int_{h^3} f_{n(p)} d\mathbf{r} d\mathbf{p}, \quad (8)$$

As the model does not consider the spin degree of freedom, the integral includes a factor of 1/2. Nonetheless, in the BUU frame, where the test particle principle is applied, the integral to calculate the phase space occupation probability is replaced by the accumulation of the contributions of the test particles. For the i th test particle at the coordinate \mathbf{r}_i and momentum \mathbf{p}_i with isospin τ_i ($= 1/2$ for the proton and $= -1/2$ for the neutron), the phase space occupation probability is expressed

as $\bar{f}(\mathbf{r}_i, \mathbf{p}_i)$,

$$\bar{f}(\mathbf{r}_i, \mathbf{p}_i) = \frac{h^3}{2N_{tp}V_p} \sum_j^{V_p, V_r} \delta(\tau_i, \tau_j) \rho_{ij}, \quad (9)$$

where V_p and V_r are the accumulating volumes around the momentum \mathbf{p}_i and coordinate \mathbf{r}_i of the i th test particle, τ_i and τ_j are the isospin of the i th and j th test particles, the δ function is for selecting the test particles with the same isospin, and ρ_{ij} is the density contribution of the j th test particle in the position of the i th test particle.

Then, the NN scattering in the model is improved, accepting two types of nucleon-nucleon scatterings. First, when all phase space occupancies at the final state are less than 1, the scattering result is accepted. In other words, we use the condition

$$\bar{f}_{in}(\mathbf{r}_i, \mathbf{p}_i) < 1, \quad \bar{f}_{fi}(\mathbf{r}_i, \mathbf{p}_i) > 1 \quad (10)$$

to block the nucleon-nucleon scattering. Here, $\bar{f}_{in}(\mathbf{r}_i, \mathbf{p}_i)$ is the phase space occupancy at the initial state and $\bar{f}_{fi}(\mathbf{r}_i, \mathbf{p}_i)$ is that at the final state. Second, when the phase space occupancy at the initial state is larger than 1, but the phase space occupancy at the final state is less than that at the initial state, the scattering result is accepted. In other words, we use the condition

$$\bar{f}_{in}(\mathbf{r}_i, \mathbf{p}_i) > 1 \quad \text{and} \quad \bar{f}_{fi}(\mathbf{r}_i, \mathbf{p}_i) > \bar{f}_{in}(\mathbf{r}_i, \mathbf{p}_i) \quad (11)$$

to block the nucleon-nucleon scattering.

In the dynamic process of the dinuclear system, the evolution of the surface plays a crucial role. We have incorporated the surface energy into the model. The surface potential is

$$U_s = g\nabla^2\rho, \quad (12)$$

where g is a parameter used to calibrate the strength of the surface potential.

The conventional BUU model is typically used to investigate reactions ranging from the Fermi energy region to the GeV energy region. For such reactions, the evolution time is typically hundreds of fm/c. This paper studies the reactions near the Coulomb barrier, where the evolution time is larger than 5000 fm/c. It is crucial to verify the stability of the model over this extended period. To this end, we simulate the evolution of the ground state of the ^{202}Po within 10^4 fm/c to test the roles of the PSDC method and surface energy. Figure 1 shows the bound mass number as a function of the evolution time without both PSDC and the surface energy (blue dotted-dashed line), without surface energy only (black dashed line), and with a surface energy parameter 2 MeV fm^5 (red solid line). Due to the model error, particle emissions occur even when simulating the evolution of a single nucleus in its ground state using the BUU model. This spurious emission effect increases over time and can cause the number of bound particles to decrease. A method is proposed to distinguish whether a particle is bound or emitted. A sphere is defined, the radius of which is $2 \times 202^{\frac{1}{3}}$ fm and the spherical center of which is the center of mass of the bound particles. Test particles within this sphere are considered bound, while those outside it are deemed emitted. The radius of the sphere is related to

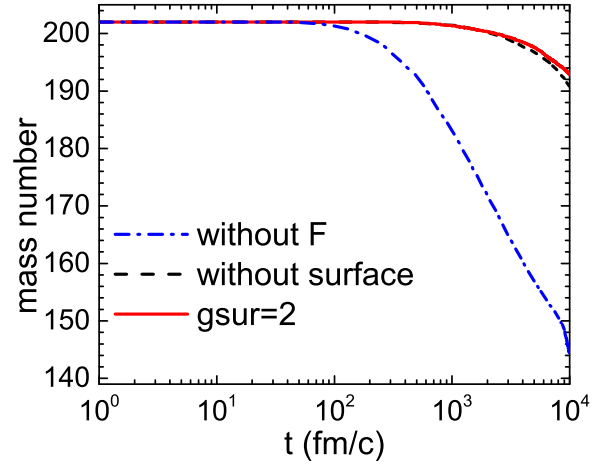


FIG. 1. Spurious emission of test particles in the BUU model. The evolution of the ground state of ^{202}Po simulated. The bound mass number as a function of the evolution time is shown in the cases without phase-space constraints (blue dotted dashed line), without surface energy constraints (black dashed line), and with surface energy parameter of 2 MeV fm^5 (red solid line).

the empirical radius of ^{202}Po $1.2 \times 202^{\frac{1}{3}}$ fm, but a value of 2 is used instead of 1.2. According to the Woods-Saxon distribution, some particles still exist outside the radius. When the calculation is performed without the PSDC method or surface energy, the spurious emissions of the particles are considered after hundreds of fm/c; see the (blue) dotted dash curve in Fig. 1. In the cases when the PSDC method is considered, the effect of the spurious emission becomes weaker. The particles in ^{202}Po in its ground state keep being bound before 10^3 fm/c; see the (red) full curve and black dashed curve in Fig. 1. During the period of evolution from 10^3 to 10^4 fm/c, about ten particles emit spuriously. The surface energy also influences the effect of the spurious emission. When the surface energy with parameter $g = 2 \text{ MeV fm}^5$ is considered, two more particles remain bound at 10^4 fm/c. In the subsequent discussion, the PSDC method will be considered and the strength of the surface energy will be adjusted.

III. RESULTS AND DISCUSSIONS

A. Window in the dinuclear system

The $^{24}\text{Mg} + ^{178}\text{Hf}$ collision at incident energy $E_{\text{lab}} = 145 \text{ MeV}$, equivalently $E^* = 79 \text{ MeV}$, or energy above the barrier $E_{\text{cm}}/V_b = 1.26$, is simulated. (E^* represents the compound nucleus excitation energy, E_{cm} represents the center-of-mass energy, and V_b the capture barrier.) The shape of the reacting system can be shown by the space distribution of the test particles. It is found that the system keeps the dinuclear shape for a long time when the collision partners dissipate their kinetic energy. To study the dissipation dynamics in the QF reaction, the window of the dinuclear system is extracted at each time step. The rotational inertia of the system is then calculated, and the long axis passing through the center of mass is determined by minimizing the rotational inertia. In other words, the long axis satisfies two conditions:

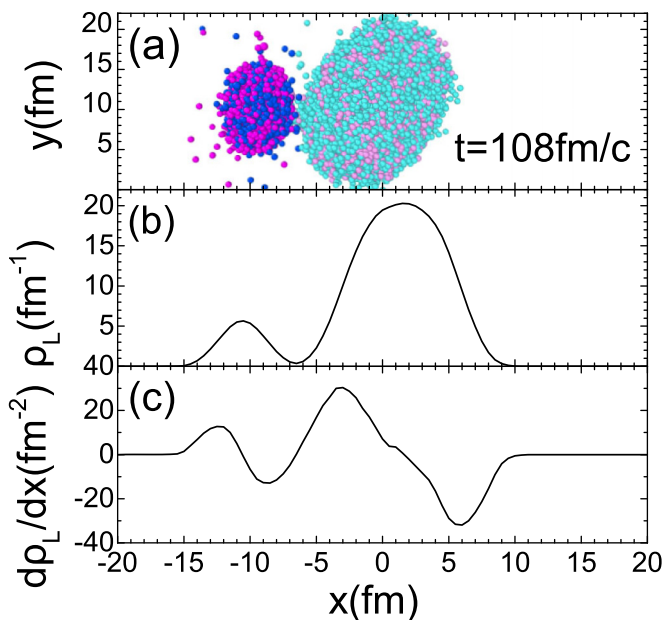


FIG. 2. (a) Space distribution of the test particles at 108 fm/c in the reaction $^{24}\text{Mg} + ^{178}\text{Hf}$ at incident energy $E_{\text{lab}} = 145$ MeV. (b) Particle density along the long axis. The long axis is defined as the axis passing through the center of mass of the system and providing the minimum value of the rotational inertia. (c) Differential coefficient of the density.

passing through the center of mass and providing the smallest moment of inertia. As an example, Fig. 2(a) shows the space distribution of the test particles at 108 fm/c when the collision partners start to touch. The moment when the projectile is 20 fm away from the target is denoted as $t = 0$ fm/c. The x axis represents the long axis of the dinuclear system, while a random axis perpendicular to the x axis is used for the y axis. The darker-colored part on the left corresponds to the projectile nuclei, whereas the lighter-colored part on the right represents the target nuclei. Protons are depicted using both light and dark blue particles, while neutrons are shown with light and dark purple particles. The initialization accounts for the deformations of the nuclei, which are preserved in the early stage of the dissipation process. The particle density distribution along the long axis is calculated and displayed in Fig. 2(b), where the unit of density is fm $^{-1}$ since it is the integrated value over the plane orthogonal to the long axis. The figure shows a bimodal distribution. The window is defined as the plane passing through the point with the minimum density and perpendicular to the long axis. Another feasible algorithm involves computing the differential coefficient of the density and searching for zero values, as demonstrated in Fig. 2(c).

Various algorithms have been proposed in the literature to describe the window in dynamic models. For mass-symmetric and central collisions, the window is described by the $z = 0$ plane and does not change during the dynamic process [39]. The window plane in collisions with finite impact parameters will rotate and move during the evolution. In Ref. [31], by employing the TDHF solutions of the rotation angle of the symmetry axis and the density distribution in the neck region, the evolution of the window plane is studied for each impact

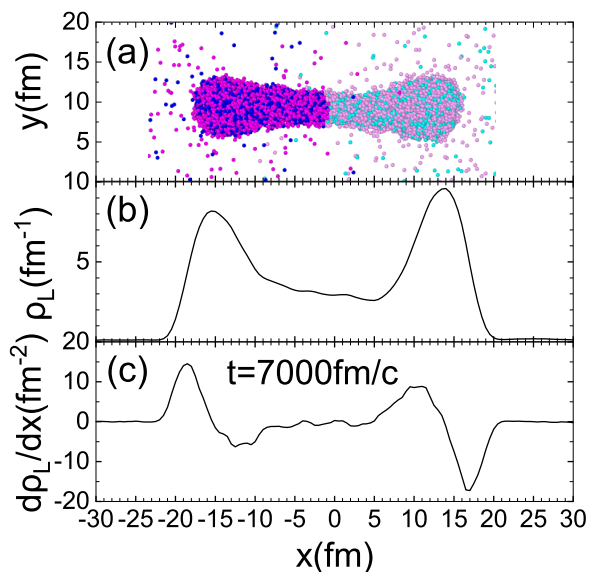


FIG. 3. Same as Fig. 2, but for the evolution time of 7000 fm/c.

parameter b . Here the window plane is perpendicular to the symmetry axis, and its center point is located at the center of the minimum density slice on the neck region. Referring to this definition, the window plane is described event-by-event in this work. For the same impact parameter b , the initial fluctuations in the phase space will be amplified due to the dissipations of the kinetic energy and angular momentum and result in the event-by-event fluctuation of the window plane.

At the later stage of the QF reaction, the window of the dinuclear system is also described. As an example, Fig. 3 shows the space distribution of test particles, the particle density along the long axis, and its differential coefficient at the moment of 7000 fm/c when the two fragments are separating. The test particles show a dumbbell shape with a long neck. In comparison to the case at 108 fm/c (see Fig. 2), the neck is longer, and more test particles are unbound. This observation indicates that the shapes of the system during the exit phase differ significantly from those during the entry phase. Here, the entry phase is defined as the stage when the distance between two fragments decreases over time, while the exit phase is contrary, i.e., distance increases over time. As shown in Fig. 3(b), the density distribution is also bimodal but with undulation in the neck region. Correspondingly, there are several local minima of the density and zero points of its differential coefficient, as shown in Fig. 3(c). It is found that any local minimum of the density may evolve into a breakpoint at the end of the QF process. Thus, the local minimum of the density is selected randomly to determine the window plane.

The window plane defined in the model plays an important role for studying the fragment observable. Particles located on the left side of the window plane belong to one fragment, whereas those on the right side belong to the other. The window acts as a partition that splits the dinuclear system into two fragments. To reveal the details of the QF process, the properties of the dinuclear system are calculated as functions of time. The mass numbers of two fragments, their distance,

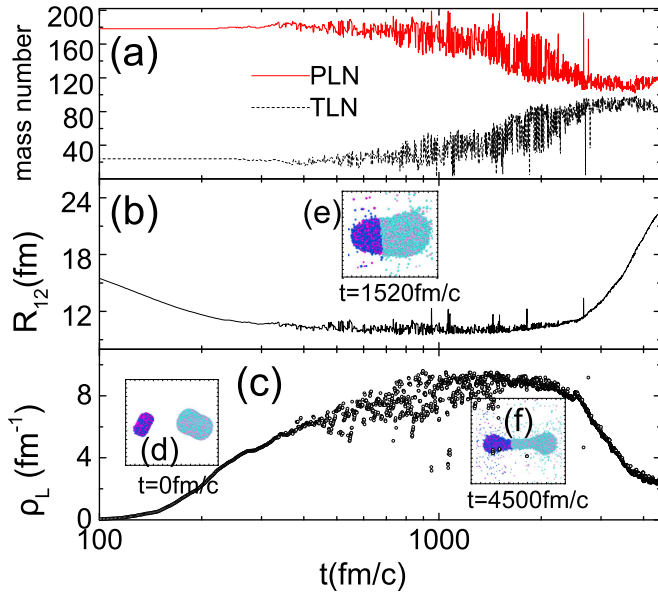


FIG. 4. (a) Mass numbers of two fragments, (b) distance between two fragments, and (c) density at the window plane as a function of time in the $^{24}\text{Mg} + ^{178}\text{Hf}$ reaction at $E_{\text{lab}} = 145$ MeV. The observables are calculated by a simulation event.

and the density at the window plane as a function of time are calculated event by event. Figure 4 shows an example. The typical dynamic characteristics of a QF event are described as follows.

From 0 to 300 fm/c. The projectile moves towards the target, and the distance between the two nuclei decreases gradually. At this stage, the two nuclei have not yet come into contact to form a dinuclear system. There is no mass transfer occurring between the projectile and the target; however, the linear density at the window increases.

From 300 to 2500 fm/c. The mass transfer between the projectile and the target begins at 300 fm/c. The mass number of the targetlike nuclei (TLN) decreases globally while that of the projectilelike nuclei (PLN) increases over time, indicating that the nucleons transfer globally from the TLN to the PLN. Here, the projectile is ^{24}Mg and the target is ^{178}Hf . During this stage, the distance between two nuclei remains almost constant, but the density at the window increases slowly. The observables are calculated by a simulation event, and hence the fluctuation is huge. As mentioned earlier, several local minima of the density could be found, and one of them is randomly selected to determine the window plane. This results in fluctuations in the window density.

From 2500 to 4500 fm/c. The mass transfer between the PLN and TLN nearly concludes after 2500 fm/c. During this stage, the mass numbers of both PLN and TLN fluctuate around a specific value. As time progresses, the distance between the two nuclei increases, and the density at the window declines. This is due to the elongation of the neck of the dinuclear system, which decreases during this period.

In the $^{24}\text{Mg} + ^{178}\text{Hf}$ reaction at $E_{\text{lab}} = 145$ MeV, three primary reaction mechanisms exist: quasi-inelastic scattering, QF, and fusion. The evolution of the window for each

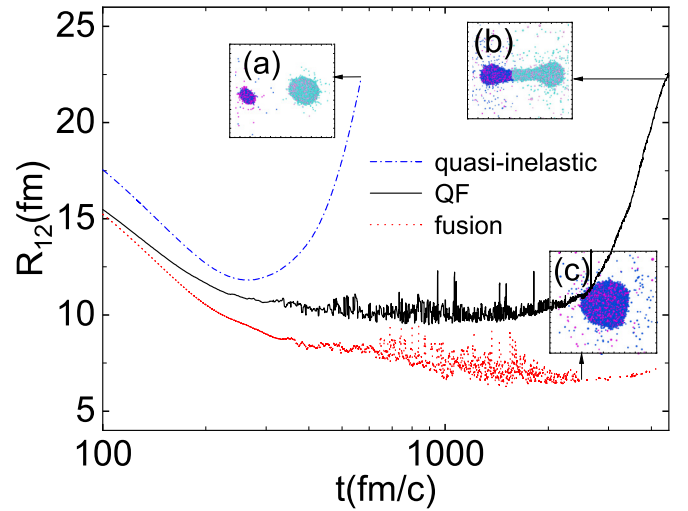


FIG. 5. The change in the distance between two nuclei over time for quasi-inelastic, QF, and fusion events for $^{24}\text{Mg} + ^{178}\text{Hf}$ collisions at $E_{\text{lab}} = 145$ MeV.

mechanism differs, enabling the possibility of distinguishing them event by event. In the case of quasi-inelastic scattering, the Coulomb barrier is not crossed, causing the two nuclei to rapidly separate after contact during the early stage. The window in quasi-inelastic events lasts for a brief period. During the early stages of QF and fusion, the Coulomb barrier is crossed, resulting in the transformation of two separated nuclei into a dinuclear system, and thus leading to a window that endures for an extended period. The duration of the window can be applied to distinguish the quasi-inelastic events. More precisely, a simulated event is a quasi-inelastic event if the density at its window has decreased to 0 fm^{-1} before 500 fm/c. The simulations of the quasi-inelastic event will be stopped at 500 fm/c.

On the other hand, the shape of the system differs between QF and fusion during the later stages of the reaction. Fusion produces a complex nucleus where the window is not identifiable, while QF leads to a tendency towards separation of the dinuclear system, causing a decrease in the density at the window over time. Whether the window can be found is applied to distinguish the QF and fusion. In fact, the dinuclear system obviously fluctuates at the end of the simulations. The observables of QF and fusion are calculated through event accumulation and time integration. More generally, the window of a simulated event is calculated during the time from 9000 to 10 000 fm/c using the algorithms shown in Figs. 2 and 3. The time steps when the window is not found contribute to the fusion events, and the other time steps contribute to the QF events. Here, “the window is not found” implies there is no local minima of the density and there are no zero points of its differential coefficient in the neck region (see Figs. 2 and 3).

Figures 5 and 6 depict the typical cases for quasi-inelastic, QF, and fusion events. In Fig. 5, the (blue) dotted-dashed line, in this case, illustrates two nuclei separating at 300 fm/c. For quasi-inelastic events, there is minimal nucleon transfer. At 550 fm/c in Fig. 5(a), the space distribution of test

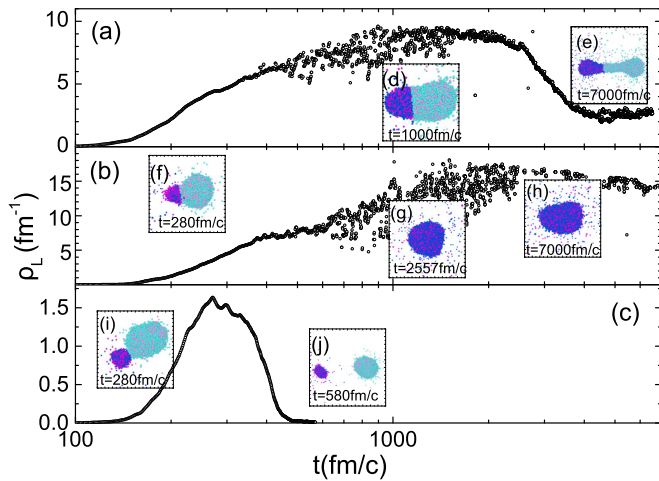


FIG. 6. Comparison of the density at the window as a function of time for (a) quasifission, (b) fusion, and (c) quasi-inelastic scattering in $^{24}\text{Mg} + ^{178}\text{Hf}$ collisions at $E_{\text{lab}} = 145 \text{ MeV}$.

particles shows that the mass numbers and deformations of both the projectile and target remain nearly unchanged after separation. The black curve represents a QF event, where the distance reaches a minimum value of 10 fm and remains constant for an extended period before the two fragments begin to move apart. The minimum of 10 fm is exactly the sum of the radii of the projectile and the target. For the fusion event, the line fluctuates from 350 fm/c, gradually decreases, and eventually settles at a value around 7 fm, which is close to the radius of the compound nucleus ^{202}Po . Figure 5(c) shows that the system is spherical without a neck.

Figure 6 displays the density at the window as functions of time for the quasi-inelastic, QF, and fusion events. The densities for the QF and fusion events, depicted in Figs. 6(a) and 6(b), respectively, reveal a steady increase until 2500 fm/c. The QF event displays a maximum density of approximately 9 fm^{-1} at the window, whereas the fusion event exhibits a higher maximum density of 18 fm^{-1} . Figure 6(d) shows that the shape of the system in the QF event evolves to a prolate ellipsoid when the window density is maximum. However, the system in the fusion event evolves to the spherical shape; see Fig. 6(g). After 2500 fm/c, the density at the window for the QF event decrease, corresponding to the elongation of the neck in the QF process. The window density representing the fusion event remains unchanged thereafter, indicating the process of the formation of the composite nucleus. For the quasi-inelastic event, depicted in Fig. 6(c), the density reaches its maximum value at 180 fm/c before dropping to 0 at 500 fm/c, signifying that the window does not form after the two nuclei come close together and then separate again.

The evolution of the distance between two nuclei and the density at the window allows for the differentiation of quasi-inelastic (marked QI) scattering, QF, and fusion (marked F) events. The prevalence of each mechanism varies depending on the impact parameter, as demonstrated in Fig. 7. The fusion occurs with a large percentage (66.3%) in central collision with $b < 1 \text{ fm}$. Its proportion decreases with increasing impact parameters. In the peripheral collision with $b > 7 \text{ fm}$,

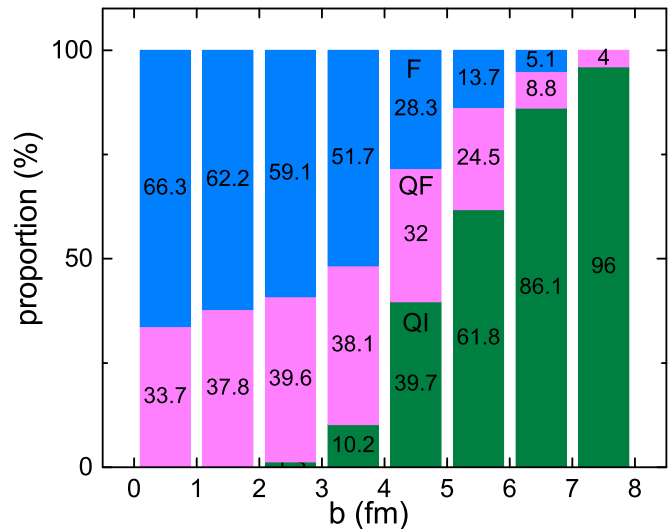


FIG. 7. Proportions of the quasi-inelastic (QI), QF, and fusion (F) events for a given impact parameter.

no fusion occurs and 96% events are for the quasi-inelastic scattering. The QF competes with fusion in collisions with small impact parameters, which is dependent on the surface energy and EOS applied in the model, as further explored later. Due to initial fluctuations in phase space accounted for by the BUU model, simulation events with the same impact parameter may bifurcate, resulting in the system evolving towards different mechanisms. For example, in collisions with impact parameters from 4 to 5 fm, the percentage is 39.7% for quasi-inelastic scattering, 32% for QF, and 28.3% for fusion. Figures 5 and 6 reveal that the first bifurcation occurs at approximately 300 fm/c, contingent on whether the Coulomb barrier is crossed (yes for quasi-inelastic scattering and no for the other two). A second bifurcation occurs at around 2500 fm/c to generate either QF or fusion.

B. Fragment observable of the quasi-fission

To investigate how the surface energy affects the reaction mechanisms, we performed the calculations with different surface energies. Specifically, the QF and fusion events were selected, and then their cross sections were calculated. Figure 8(a) presents the resulting total capture, QF, and fusion cross sections as a function of the surface parameter employed in the model. The surface energy works to minimize the surface area of the system. In the early stage of the collision, the surface energy suppresses the deformation of the projectile and target and hence raises the dynamics barrier. So the capture cross section decreases with increasing surface parameter g ; see (blue) triangles in Fig. 8(a). Conversely, once the barrier is surpassed and the nuclei significantly overlap, the surface energy drives shape evolution towards a sphere, hindering the separation of the two parts. As such, while the cross section of QF decreases with increasing surface parameter g , that of fusion increases, represented respectively by the (black) squares and (red) circles in Fig. 8(a).

Regarding QF events, the window plane at the end of simulations divides the system into two fragments, including

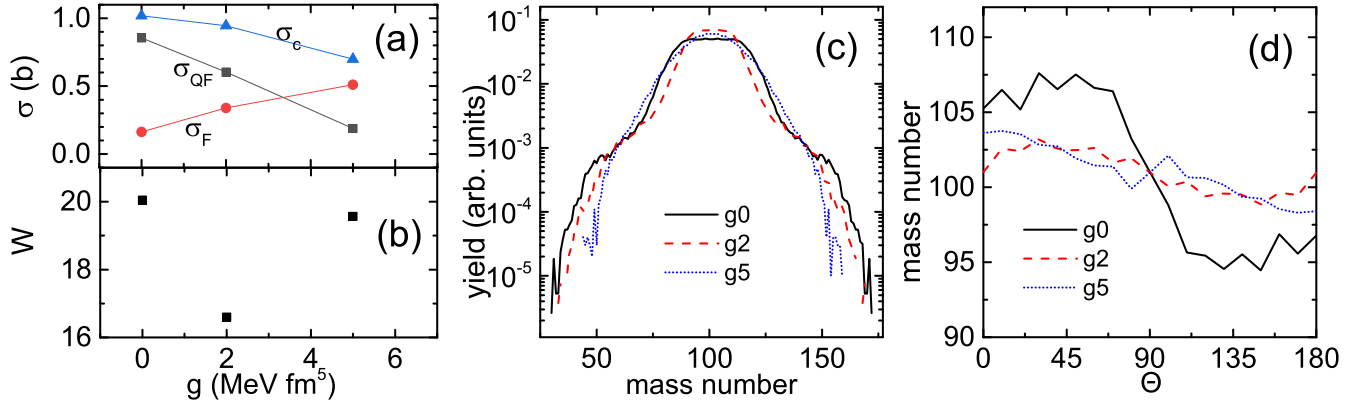


FIG. 8. (a) Calculated cross section of the total capture (blue triangles), QF (black squares), and fusion (red circles) as a function of the surface parameter g applied in the BUU model. (b) Widths of the mass distribution for QF events as a function of the surface parameter g . (c) Mass distributions and (d) the mass-angular correlations of the fragments for QF events calculated within different surface parameters g .

any test particles that have emitted spuriously. In this case, the error derived from the spurious emissions of the particles is reduced. The mass number and emission angle of the fragments in QF events are calculated event by event. The widths of the mass distributions as functions of the surface parameter applied in the model are depicted in Fig. 8(b). These widths rapidly decrease before increasing with increasing surface parameters due to competition between long- and short-lived QFs. In the works by Williams *et al.* and Wakhle *et al.* [52,53], the QF events were divided into the long-lived and short-lived cases according to the sticking time between the PLN and the TLN. The long-lived QF is mass symmetric, which results in the Gaussian distribution of around half the mass of the system. However, in the short-lived QF, the mass equilibrium is not achieved, but the mass transfer is considerable, leading to two separate Gaussian shapes in the mass distribution.

In Fig. 8(c), the reduced mass distributions of the fragments produced in the QF events are shown. In the mass distribution calculated without the surface energy, the components of the long- and short-lived QFs can be distinguished; see the black curve in Fig. 8(c). The main contribution is the distribution around 101 caused by the long-lived QF, while the short-lived QF, which accounts for only about one-thousandth of simulated events, causes apophyses in the mass distribution around the mass numbers of 50 and 150. Comparing the black curve and the (red) dashed curve in Fig. 8(c), the surface energy applied in the model affects the mass distribution in three ways: reducing the contribution of the short-lived QF, shifting the components of the short-lived QF towards the symmetric axis ($A = 101$), and narrowing the component of the long-lived QF. Strong surface energy eliminates the distinction between long- and short-lived QFs, exemplified by the (blue) dots in Fig. 8(c) for $g = 5$ MeV fm⁵, wherein a single wide Gaussian shape represents the mass distribution.

The average mass number of the fragments emitting at a given angle can be applied to investigate the rotation of the system in the QF process. Here, the angle is for the center-of-mass frame. Generally, the fragments produced in a central collision ($b = 0$ fm) will emit at 0° and 180°, indicating no rotation since the initial angular momentum is zero. Figure 8(d) shows the mass-angular correlations of the fragments for QF

events with different surface parameters g . The ordinate variable is calculated by integrating the fragment mass in each 0.1 cosine of the angle. The figure reveals that the average mass number of fragments emitting at 0° is larger than 101, while that at 180° is less than 101, implying that mass balance is not achieved for QF events in central collisions. On the other hand, comparing three curves in the figure, it is found that the mass number of two fragments at 0° and 180° is more symmetric after the surface energy is applied in the model. The surface energy enhances the contact time of the dinuclear system, leading to more nucleons transferring from the target to the projectile. As impact parameter increases, the colliding system possesses greater angular momentum and rotates more. Fragments at front angles consistently exhibit larger average mass numbers than those at back angles, suggesting that front angle fragments are targetlike nuclei and back angle fragments are projectilelike nuclei. It seems that the rotation angle of the system is less than 90°. The statistical error is quite large so that the difference of the calculations within surface parameters 2 and 5 MeV fm⁵ is not observed.

Not only does surface energy, but the incompressibility K of the nuclear EOS also influences dissipation dynamics in QF reactions. As is well known, soft nuclear matter gives way to pressure easily, akin to clay, while a hard EOS suppresses deformation of the projectile and target, thereby raising the dynamics barrier. The (blue) triangles in Fig. 9(a) show that the capture cross section decreases slowly with increasing incompressibility of the nuclear EOS applied in the model, indicating weak effects of incompressibility on the dynamics barrier. On the other hand, the competition between the QF and fusion depends on the incompressibility of the EOS applied in the model. One sees the cross section of QF decrease, but that of fusion increases with increasing incompressibility K of the EOS. See (black) squares and (red) circles, respectively, in Fig. 9(a).

The mass distribution of the fragments produced in QF events depends on the incompressibility of the EOS. Figure 9(b) shows that the width of the distribution increases from 16.5 to 21.8 with increasing incompressibility K from 200 to 271 MeV. Details are evident in Fig. 9(c), which displays the mass distributions for the QF events for

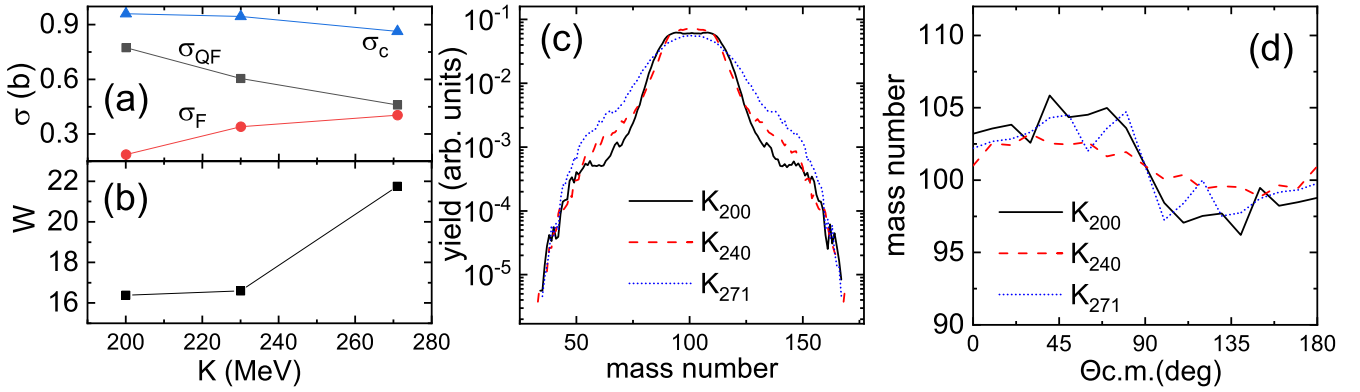


FIG. 9. Same as Fig. 8 but for different incompressibility K applied in the BUU model.

different incompressibilities. Here, the surface parameter $g = 2 \text{ MeV fm}^5$ is applied, and the components of the long- and short-lived QFs can be distinguished for all cases with different incompressibility. The apophyses in the mass distributions around $A = 50$ and 150 are caused by the short-lived QF. Their locations are independent of the incompressibility, but their yields increase with increasing incompressibility. The yield at $A = 50$ for $K = 271 \text{ MeV}$ is about triple that for $K = 200 \text{ MeV}$. The long-lived QF contributes to the Gaussian shape around $A = 101$. The widths increase with increasing incompressibility. Figure 9(d) shows the average mass number of the fragments as a function of the emitting angle. The effects of incompressibility are not observed within the statistical errors.

The effects of the surface energy and incompressibility on the QF process can be investigated by showing the mass-angular correlations of the fragments produced in collisions at different impact parameters; see Fig. 10. Panels (a) to (d) show the calculations with parameters $K = 240 \text{ MeV}$ and $g = 0$, panels (e) to (h) for $K = 240 \text{ MeV}$ and $g = 2 \text{ MeV fm}^5$, and panels (i) to (l) for $K = 271 \text{ MeV}$ and $g = 2 \text{ MeV fm}^5$. Colors represent probabilities in mass-angular correlations proportional to differential cross section $\frac{d\sigma}{dA d\theta}$. Figure 10(a) shows that the angles of the fragments produced in the central collision are close to 0° or 180° , but their masses are distributed in the region from 80 to 122. The QF is asymmetric in this case. With increasing impact parameter, the most probable mass remains almost constant, but the most probable angle moves from 0° (or 180°), see Fig. 10(a), to 40° (or 135°), see Fig. 10(d). In the peripheral collision, the angular momentum is larger, and the dinuclear system rotates more compared to the central collision. However, fluctuation of angles does not monotonically increase over the impact parameter. The widest angle distribution is observed in collisions with $b = 5\text{--}6 \text{ fm}$, indicating the strongest dissipation of the angular momentum.

By comparing the calculations with and without the surface energy, the effect of the surface energy on the dissipations of the mass and angular momentum can be found. The QF simulated without surface energy is asymmetric. However, after the surface energy of 2 MeV fm^5 is applied, the mass transfer between the collision partners increases, and the QF tends to be symmetric. The masses of both fragments

are distributed in the region around $A = 101$, as shown in Figs. 10(e)–10(h). For identical impact parameters, calculated distributions with surface energy have more probable angles closer to 90° than those without surface energy, indicating that surface energy enhances contact time and dinuclear system rotation. For example, they are 30° and 150° in Fig. 10(e) but 0° and 180° in Fig. 10(a). Moreover, after the surface energy is applied, the event fluctuation of the mass is enhanced slightly, but that of the angle is clearly reduced. According to the theorem that the fluctuation is caused by the dissipation, the surface energy inhibits the angular momentum dissipation.

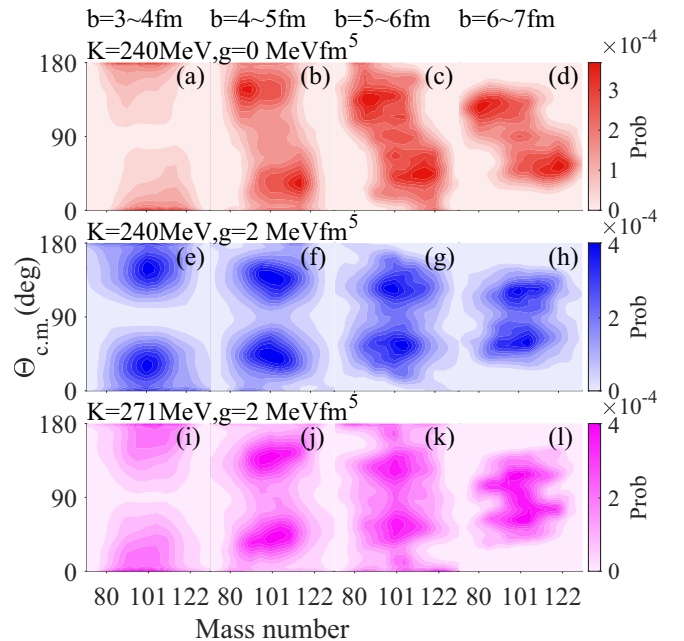


FIG. 10. Mass-angular correlations of the fragments produced in collisions at different impact parameters. Panels (a)–(d) show the calculations with parameters $K = 240 \text{ MeV}$ and $g = 0$, panels (e)–(h) for $K = 240 \text{ MeV}$ and $g = 2 \text{ MeV fm}^5$, and panels (i)–(l) for $K = 271 \text{ MeV}$ and $g = 2 \text{ MeV fm}^5$. The colors display the probability in the mass-angular correlations proportional to the differential cross section $\frac{d\sigma}{dA d\theta}$.

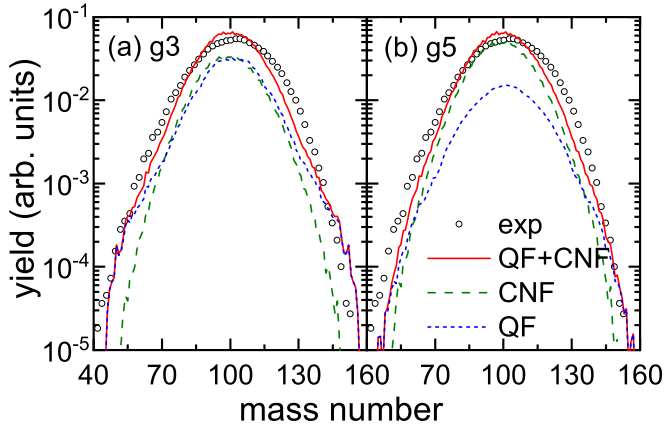


FIG. 11. Mass distribution of the fragments produced in $^{24}\text{Mg} + ^{178}\text{Hf}$ at $E_{\text{lab}} = 145$ MeV. The circles are the experimental data from Ref. [40]. The (red) lines are the calculations in this work. The (blue) dots and (green) dashes show the contributions of the QF and CNF events.

By comparing calculations in Figs. 10(i)–10(l) to those in Figs. 10(e)–10(h), the effect of the incompressibility can be found. The incompressibility from 240 to 271 MeV does not affect the most probable mass for all impact parameters but enhances event fluctuation of the mass distribution. The dependence of the angle distribution on the incompressibility is complex. For the collisions with $b = 3\text{--}4$ fm, the larger incompressibility reduces the rotation of the dinuclear system and inhibits the event fluctuation of the angle; see Figs. 10(e) and 10(i). However, for the collisions with $b = 5\text{--}6$ fm, the rotations of the system are similar for both calculations with different incompressibilities, and the event fluctuation of the angle is larger when a larger incompressibility is applied.

C. Comparison between calculation and data

Fusion results in a complex nucleus, and compound nucleus fission (CNF) events are simulated using the GEMINI++ code. Mass number and emissions angle are calculated for CNF events. The fragment observable in the $^{24}\text{Mg} + ^{178}\text{Hf}$ reaction at $E_{\text{lab}} = 145$ MeV is the summation with the weighting of the QF and fusion cross sections. In fact, the mass distribution and mass-angular correlation of the fragments in the $^{24}\text{Mg} + ^{178}\text{Hf}$ reaction at $E_{\text{lab}} = 145$ MeV have been measured experimentally [54]. Identifying contributions of QF and CNF reactions to the fragment observable presents a challenge since the data are mixed distributions for QF and CNF reactions. However, the BUU model clearly distinguishes between QF and CNF events, enabling investigation of their individual contributions by examining mass distribution and mass-angular correlation.

Calculations with incompressibility of 240 MeV and surface parameter $g = 3$ and 5 MeV fm^5 agree with the data on mass distribution, as seen in Fig. 11. The (red) lines in the figures are for the mixture distributions, which agree to the data globally. The (blue) dots and (green) dashes show the contributions of the QF and CNF events. Both distributions

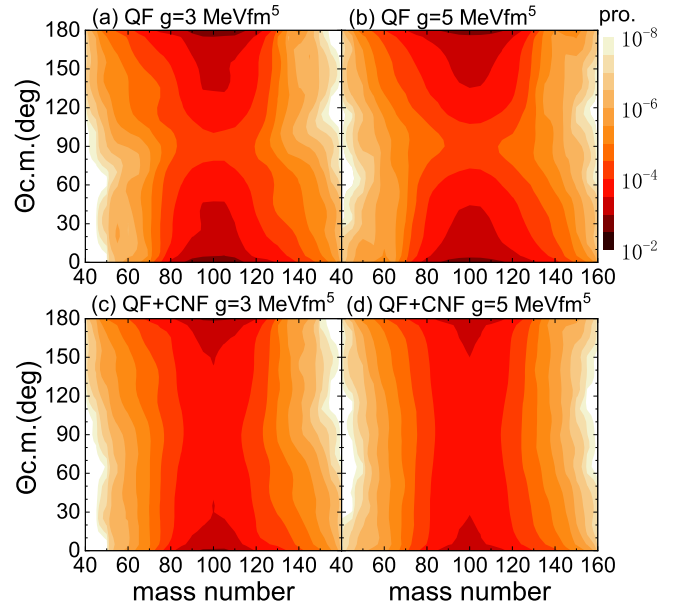


FIG. 12. Mass-angular correlation of the fragments. Panels (a) and (b) are for the QF events with surface parameter values $g = 3$ and $g = 5 \text{ MeV fm}^5$, respectively. Panels (c) and (d) are for the mixture of QF and CNF events with the surface parameter values $g = 3$ and $g = 5 \text{ MeV fm}^5$, respectively. The colors display the probability in the mass-angular correlations proportional to the differential cross section $\frac{d\sigma}{dA d\theta}$.

display a Gaussian shape with similar widths. It can be seen from Fig. 11(a) that the contributions of QF and CNF reactions to the mass distribution are similar when the surface parameter $g = 3 \text{ MeV fm}^5$ is applied in the calculations. However, the calculations for $g = 5 \text{ MeV fm}^5$ show that the CNF events play a main role in $^{24}\text{Mg} + ^{178}\text{Hf}$ reaction at $E_{\text{lab}} = 145$ MeV, which supports the viewpoint in Ref. [40].

The calculated mass-angular correlations for QF events with the surface parameter values $g = 3$ and 5 MeV fm^5 are shown in Figs. 12(a) and 12(b). Colors represent probabilities in mass-angular correlations proportional to differential cross section $\frac{d\sigma}{dA d\theta}$. Both calculations reveal that the differential cross sections at the angles 0° and 180° are larger than that at 90° . Furthermore, the fragments emitting at the front angle ($< 90^\circ$) are targetlike fragments and those at back angle ($> 90^\circ$) are projectilelike fragments. The mass-asymmetry and the nonisotropic emission of the fragments are characteristic of the QF process. However, this characteristic may be covered by the CNF events, in which fragments exhibit mass symmetry and isotropic emission. The calculated mass-angular distributions for QF and CNF events are added with the weighting of the QF and fusion cross sections and shown in Figs. 12(c) and 12(d). Since the contributions of QF and CNF events are similar when $g = 3 \text{ MeV fm}^5$ [see Fig. 11(a)], the mass-angular distribution in Fig. 12(c) still displays the characteristics of the mass asymmetry and the nonisotropic emission. However, the mass-angular distribution calculated within the surface parameter $g = 5 \text{ MeV fm}^5$ is mass symmetric and nearly isotropic, which agrees with experimental

data in Ref. [11]. It is deduced that the CNF events play the main role and accounts for the characteristic of fragment observables in the $^{24}\text{Mg} + ^{178}\text{Hf}$ reaction at $E_{\text{lab}} = 145$ MeV.

IV. CONCLUSION

The Boltzmann-Uehling-Uhlenbeck model is improved to study the heavy-ion collision at incident energy near the Coulomb barrier. The $^{24}\text{Mg} + ^{178}\text{Hf}$ reaction at $E_{\text{lab}} = 145$ MeV is investigated by the model. A new method has been raised to separate the quasi-inelastic, quasifission, and fusion events. Specifically, the window plane of the dinuclear system is defined, and its time evolution is extracted event by event. The evolution of the distance between the two fragments and the density at the window is different for the quasi-inelastic, quasifission, and fusion events. Thus these three mechanisms can be distinguished by this method. The proportions of the three mechanisms are calculated. It is shown that fusion occurs with a large percentage in central collisions, and quasi-inelastic scattering occurs mainly in peripheral collisions. Quasi-fission competes with fusion in collisions with a small impact parameter. The effects of the surface energy and the incompressibility on the reaction mechanisms are studied. It is found that the cross section of the quasifission decreased, and that of the fusion increased with increasing surface energy and incompressibility.

The mass distributions and mass-angular correlations of the fragments in quasifission and fusion events are calculated and compared. It is shown that the global mass distribution of the fragments for both mechanisms is symmetric along the half mass of the system. However, the mass-angular correlation of the quasifission events shows mass asymmetry. The fragments emitting at front angle ($<90^\circ$) are targetlike fragments and those at back angle ($>90^\circ$) are projectilelike fragments. Furthermore, the differential cross sections at the angles 0° and 180° are larger than that at 90° . It is indicated that the mass-asymmetry and the nonisotropic emission of the fragments are the characteristics of quasifission, which support the viewpoint that the incident energy in the quasi-fission is not entirely dissipated. By comparing the calculations of the mass distribution and mass-angular correlation to the data, it is deduced that compound nucleus fission plays the main role and accounts for the characteristic of fragment observables in the $^{24}\text{Mg} + ^{178}\text{Hf}$ reaction at $E_{\text{lab}} = 145$ MeV.

ACKNOWLEDGMENTS

This work was supported by the National Natural Science Foundation of China under Grants No. 11875328 and No. 12075327 and by the Fundamental Research Funds for the Central Universities, Sun Yat-Sen University (No. 221gqb39).

-
- [1] J. Töke, R. Bock, G. Dai, A. Gobbi, S. Gralla, K. Hildenbrand, J. Kuzminski, W. Müller, A. Olmi, H. Stelzer *et al.*, *Nucl. Phys. A* **440**, 327 (1985).
- [2] B. Back, *Phys. Rev. C* **31**, 2104 (1985).
- [3] W. Swiatecki, *Phys. Scr.* **24**, 113 (1981).
- [4] H. C. Manjunatha, L. Seenappa, P. S. Damodara Gupta, N. Manjunatha, K. N. Sridhar, N. Sowmya, and T. Nandi, *Phys. Rev. C* **103**, 024311 (2021).
- [5] N. Kumar, D. C. Biswas, T. K. Ghosh, J. Sadhukhan, B. N. Joshi, Y. K. Gupta, R. P. Vind, G. K. Prajapati, S. Dubey, L. S. Danu, S. Mukhopadhyay, K. Mahata, B. V. John, and S. Sodaye, *Phys. Rev. C* **99**, 041602(R) (2019).
- [6] G. Adamian, N. Antonenko, and S. A. Kalandarov, *Phys. Part. Nuclei* **47**, 1 (2016).
- [7] R. du Rietz, E. Williams, D. J. Hinde, M. Dasgupta, M. Evers, C. J. Lin, D. H. Luong, C. Simenel, and A. Wakhle, *Phys. Rev. C* **88**, 054618 (2013).
- [8] E. M. Kozulin, G. N. Knyazheva, I. M. Itkis, M. G. Itkis, A. A. Bogachev, E. V. Chernysheva, L. Krupa, F. Hanappe, O. Dorvaux, L. Stuttgé, W. H. Trzaska, C. Schmitt, and G. Chubarina, *Phys. Rev. C* **90**, 054608 (2014).
- [9] E. M. Kozulin, G. N. Knyazheva, S. N. Dmitriev, I. M. Itkis, M. G. Itkis, T. A. Loktev, K. V. Novikov, A. N. Baranov, W. H. Trzaska, E. Vardaci, S. Heinz, O. Beliuskina, and S. V. Khlebnikov, *Phys. Rev. C* **89**, 014614 (2014).
- [10] E. Vardaci, A. Pulcini, E. M. Kozulin, I. Matea, D. Verney, A. Maj, C. Schmitt, I. M. Itkis, G. N. Knyazheva, K. Novikov, N. Kozulina, I. M. Harca, I. V. Kolesov, K. Saveleva, V. V. Kirakosyan, O. Dorvaux, M. Ciemala, S. Brambilla, M. Ashaduzzaman, B. DeCanditiis, A. DiNitto, D. Quero, C. Parascandolo, D. Pierroutsakou, P. K. Rath, G. Sposito, G. LaRana, A. Bracco, F. Camera, O. Stezowski, C. Borcea, S. Calinescu, C. Petrone, and J. Wilson, *Phys. Rev. C* **101**, 064612 (2020).
- [11] C. Schmitt, K. Mazurek, and P. N. Nadtochy, *Phys. Rev. C* **100**, 064606 (2019).
- [12] A. Sen, T. K. Ghosh, E. M. Kozulin, I. M. Itkis, G. N. Knyazheva, K. V. Novikov, S. Bhattacharya, K. Banerjee, and C. Bhattacharya, *Phys. Rev. C* **105**, 014627 (2022).
- [13] E. M. Kozulin, G. N. Knyazheva, A. A. Bogachev, V. V. Saiko, A. V. Karpov, I. M. Itkis, K. V. Novikov, Y. S. Mukhamejanov, I. V. Pchelintsev, I. V. Vorobiev, T. Banerjee, M. Cheralu, and P. P. Singh, *Phys. Rev. C* **105**, 024617 (2022).
- [14] E. Prasad, A. Wakhle, D. J. Hinde, E. Williams, M. Dasgupta, M. Evers, D. H. Luong, G. Mohanto, C. Simenel, and K. Vo-Phuoc, *Phys. Rev. C* **93**, 024607 (2016).
- [15] C. J. Lin, R. du Rietz, D. J. Hinde, M. Dasgupta, R. G. Thomas, M. L. Brown, M. Evers, L. Gasques, and M. D. Rodriguez, *Phys. Rev. C* **85**, 014611 (2012).
- [16] M. Itkis, A. Bogachev, I. Itkis, J. Kliman, G. Knyazheva, N. Kondratiev, E. Kozulin, L. Krupa, Y. Ts. Oganessian, I. Pokrovsky *et al.*, *Dynamical Aspects of Nuclear Fission* (World Scientific, Singapore, 2008), pp. 36–53.
- [17] A. Diaz-Torres, G. G. Adamian, N. V. Antonenko, and W. Scheid, *Phys. Rev. C* **64**, 024604 (2001).
- [18] X. J. Bao *et al.*, *Phys. Rev. C* **102**, 054613 (2020).
- [19] S. Chopra, M. K. Sharma, P. O. Hess, Hemdeep, and Neetu-Maan, *Phys. Rev. C* **103**, 064615 (2021).
- [20] N. Kumari, A. Deep, and R. Kharab, *Phys. Rev. C* **105**, 014628 (2022).

- [21] P. A. Dirac, *Math. Proc. Cambridge Philos. Soc.* **26**, 376 (1930).
- [22] L. Li, L. Guo, K. Godbey, and A. Umar, *Phys. Lett. B* **833**, 137349 (2022).
- [23] N. Wang and L. Guo, *Phys. Lett. B* **760**, 236 (2016).
- [24] S. Ayik, *Phys. Lett. B* **658**, 174 (2008).
- [25] G. Zhang, J.-J. Li, X.-R. Zhang, B. Li, C. A. T. Sokhna, C. Wang, Z. Liu, and F.-S. Zhang, *Phys. Rev. C* **102**, 024617 (2020).
- [26] L. Zhu and J. Su, *Phys. Rev. C* **104**, 044606 (2021).
- [27] M. K. Sharma, S. Kanwar, G. Sawhney, R. K. Gupta, and W. Greiner, *J. Phys. G: Nucl. Part. Phys.* **38**, 055104 (2011).
- [28] C. Simenel, D. Hinde, R. Du Rietz, M. Dasgupta, M. Evers, C. Lin, D. Luong, and A. Wakhle, *Phys. Lett. B* **710**, 607 (2012).
- [29] V. E. Oberacker, A. S. Umar, and C. Simenel, *Phys. Rev. C* **90**, 054605 (2014).
- [30] X. Jiang, S. Yan, and J. A. Maruhn, *Phys. Rev. C* **88**, 044611 (2013).
- [31] S. Ayik, B. Yilmaz, O. Yilmaz, and A. S. Umar, *Phys. Rev. C* **97**, 054618 (2018).
- [32] C. Li, J. Tian, and F.-S. Zhang, *Phys. Lett. B* **809**, 135697 (2020).
- [33] S. Ayik and K. Sekizawa, *Phys. Rev. C* **102**, 064619 (2020).
- [34] K. Davies, A. Sierk, and J. Nix, *Phys. Rev. C* **13**, 2385 (1976).
- [35] H. Zheng, S. Burrello, M. Colonna, D. Lacroix, and G. Scamps, *Phys. Rev. C* **98**, 024622 (2018).
- [36] I. Ulgen, B. Yilmaz, and D. Lacroix, *Phys. Rev. C* **100**, 054603 (2019).
- [37] S. Pal and N. Ganguly, *Nucl. Phys. A* **370**, 175 (1981).
- [38] S. Tanaka, Y. Aritomo, Y. Miyamoto, K. Hirose, and K. Nishio, *Phys. Rev. C* **100**, 064605 (2019).
- [39] K. Wen, F. Sakata, Z.-X. Li, X.-Z. Wu, Y.-X. Zhang, S.-G. Zhou *et al.*, *Phys. Rev. Lett.* **111**, 012501 (2013).
- [40] R. Rafiei, R. G. Thomas, D. J. Hinde, M. Dasgupta, C. R. Morton, L. R. Gasques, M. L. Brown, and M. D. Rodriguez, *Phys. Rev. C* **77**, 024606 (2008).
- [41] D. Durand, E. Suraud, and B. Tamain, *Nuclear Dynamics in the Nucleonic Regime* (CRC, Boca Raton, 2000).
- [42] H. Reinhardt, P.-G. Reinhard, and K. Goeke, *Phys. Lett. B* **151**, 177 (1985).
- [43] P. Reinhard, H. Reinhardt, and K. Goeke, *Ann. Phys. (NY)* **166**, 257 (1986).
- [44] P.-G. Reinhard and E. Suraud, *Ann. Phys. (NY)* **354**, 183 (2015).
- [45] P. M. Dinh, M. Vincendon, F. Coppens, E. Suraud, and P.-G. Reinhard, *Comput. Phys. Commun.* **270**, 108155 (2022).
- [46] G. Bertsch and S. D. Gupta, *Phys. Rep.* **160**, 189 (1988).
- [47] J. Aichelin and G. Bertsch, *Phys. Rev. C* **31**, 1730 (1985).
- [48] H. Kruse, B. V. Jacak, and H. Stöcker, *Phys. Rev. Lett.* **54**, 289 (1985).
- [49] C. Grégoire, B. Remaud, F. Sébille, L. Vinet, and Y. Raffray, *Nucl. Phys. A* **465**, 317 (1987).
- [50] J. Cugnon, D. L'Hôte, and J. Vandermeulen, *Nucl. Instrum. Methods Phys. Res. Sect. B* **111**, 215 (1996).
- [51] C. Xiangzhou, F. Jun, S. Wenqing, M. Yugang, W. Jiansong, and Y. Wei, *Phys. Rev. C* **58**, 572 (1998).
- [52] A. Wakhle, C. Simenel, D. J. Hinde, M. Dasgupta, M. Evers, D. H. Luong, R. du Rietz, and E. Williams, *Phys. Rev. Lett.* **113**, 182502 (2014).
- [53] E. Williams, D. J. Hinde, M. Dasgupta, R. du Rietz, I. P. Carter, M. Evers, D. H. Luong, S. D. McNeil, D. C. Rafferty, K. Ramachandran, and A. Wakhle, *Phys. Rev. C* **88**, 034611 (2013).
- [54] T. Banerjee, D. J. Hinde, D. Y. Jeung, K. Banerjee, M. Dasgupta, A. C. Berriman, L. T. Bezzina, H. M. Albers, C. E. Düllmann, J. Khuyagbaatar, B. Kindler, B. Lommel, E. C. Simpson, C. Sengupta, B. M. A. Swinton-Bland, T. Tanaka, A. Yakushev, K. Eberhardt, C. Mokry, J. Runke, P. Thorle-Pospiech, and N. Trautmann, *Phys. Rev. C* **102**, 024603 (2020).